Progress in Additive Manufacturing (2022) 7:1195–1212
https://doi.org/10.1007/s40964-022-00294-7

FULL RESEARCH ARTICLE

Relationship between microstructure, mechanical and magnetic properties of pure iron produced by laser powder bed fusion (L-PBF) in the as-built and stress relieved conditions

Mattia Zanni[1] · Lorella Ceschini[1] · Alessandro Fortunato[1] · Giuseppe Valli[1] · Lucia Del Bianco[2] · Federico Spizzo[2]

Received: 16 November 2021 / Accepted: 27 March 2022 / Published online: 15 April 2022

Abstract
In the present work, the mechanical and magnetic properties of pure iron manufactured by laser-powder bed fusion (L-PBF) were investigated both in the as-built (AB) and stress relieved (HT) conditions, with the aim of elucidating their relationship with the microstructure and evaluating whether and to what extent it can be suitable for industrial applications. The L-PBF process was optimized to obtain high density, crack-free components. Specimens for microstructural analyses, tensile and magnetic tests were manufactured under the optimized conditions and tested both in the as-built and annealed (850 °C for 1 h, to relieve the residual stresses) conditions. Tensile tests showed high tensile strength in both AB and HT conditions (larger than those of conventionally produced pure iron), with higher ductility and lower strength after stress relieving. The magnetic study indicated a not optimal magnetic softness although the heat treatment enhanced the permeability and reduced the coercivity with respect to the as-built condition. The high mechanical strength and low magnetic softness came from the very fine grain size (about 5 μm) of L-PBF pure iron. Instead, the improvement of magnetic softness and ductility after heat treatment was attributed to the possible reduction of dislocation density and consequent stress relief. The results indicated the possibility to achieve a considerably high mechanical strength, in pure iron manufactured by L-PBF, although the fine grain size limits its magnetic softness.

Keywords Laser powder bed fusion (L-PBF) · Pure iron · Soft magnetic properties · Tensile strength

1 Introduction

Magnetically soft materials represent a special class of materials which can be easily magnetized through the application of weak magnetic fields [1, 2]. The main requirements for a good magnetic softness are high magnetic permeability and saturation polarization. Low magnetic coercivity and remanence are also required, as well as high electrical resistivity for AC applications. These properties result in low hysteresis and eddy-current energy losses, hence magnetically soft materials are typically used for applications involving electromagnetic induction cycling, such as transformers, electric motors and generators and for the fabrication of electromagnets and yokes, as well as magnetic shields [1, 2]. Typically, magnetically soft materials are commercially available in form of thin sheets and strips, produced by hot and cold rolling. Sheets and strips are pierced and blanked to the desired shape and then stacked and joined to obtain the final component [3]. After this step, the material undergoes a proper heat treatment to enhance the magnetic properties that, similarly to the mechanical ones, are strongly affected by several microstructural features, which can be modified by means of cold working and adequate heat treatments [1, 2]. Residual stresses, grain boundaries and lattice defects, such as dislocations or interstitial atoms, hinder the motion of magnetic domains, thus worsening the soft magnetic behaviour. For these reasons, a final heat treatment is generally performed after the piercing and blanking operations to relief the residual stresses, to reduce the density of dislocations, and eventually to induce grain growth, aiming to minimize the obstacles to the motion of magnetic domains [1, 2].

✉ Mattia Zanni
mattia.zanni2@unibo.it

[1] Department of Industrial Engineering (DIN), Alma Mater Studiorum, University of Bologna, Viale Risorgimento 4, 40136 Bologna, Italy

[2] Department of Physics and Earth Science, University of Ferrara, Via Saragat 1, 44122 Ferrara, Italy

Different metals and alloys exhibit soft magnetic behaviour, such as pure iron, nickel–iron and iron-silicon alloys (also known as electrical steels, hereafter indicated as Fe-Si). The use of high-purity iron as a magnetically soft material is restricted to some DC applications due to its low electrical resistivity, which results in high energy losses in AC applications. Moreover, pure iron is characterized by low mechanical strength when manufactured by conventional manufacturing processes. ARMCO® pure iron [4] is a typical example of commercially available high purity iron exploited for soft magnetic applications [5]. Instead, alloys characterized by higher electrical resistivity and magnetic softness, such as Fe-Si alloys, are widespread to produce electric devices also for AC applications.

To date, new manufacturing technologies potentially able to overcome the limitations of conventional processes, such as additive manufacturing (AM), are of a great interest for a variety of applications. The term additive manufacturing (AM) indicates a group of technologies that enable the production of components directly from a 3D model by joining material, usually layer-upon-layer [6]. Among the different AM technologies, laser-powder bed fusion (L-PBF) builds near-net shape components by selectively melting thin layers of metal powder (typically from 20 to 100 µm in size) using a laser beam as focused heat source. L-PBF is one of the most consolidated AM technology for metals and enables the production of complex components, with cavities and shapes not achievable with traditional technologies, thus also enabling the use of topology optimization design methods [7–13]. Topology optimization generates optimized structures by adding or removing material in the design domain with the target of maximize a specific feature, for example weight reduction or magnetic flux [14–16]. The geometries obtained by topology optimization are generally complex and difficult to be manufactured by conventional processes, such as casting or subtractive techniques, and require innovative AM technologies such as L-PBF. Several literature works [17–28] addressed the L-PBF manufacturing of magnetically soft materials, in particular Fe-Si alloys with high Si content (up to 6.9 wt%) in view of their promising magnetic behaviour and possible applications. However, the L-PBF process of Fe-Si alloys is still challenging due to their high cracking tendency and brittleness, which prevent the manufacturing of high density, crack-free components [17, 20, 21]. On the contrary, literature studies [29–33] proved the L-PBF feasibility of commercial pure iron, reporting the possibility to produce crack-free parts. It is worth mentioning that, in general, the microstructure of metals manufactured by L-PBF strongly differs from that of cast and wrought ones. The peculiar solidification conditions of the L-PBF process often result in a specific microstructure, defined as hierarchical, composed of large and columnar grains oriented along the building direction (vertical direction), melt pools and scan tracks borders, and a fine-sized, cellular-dendritic substructure [7–11]. However, previous works from several authors [29–33] highlighted that the as-built microstructure of pure iron processed via L-PBF consists of fine-sized, randomly oriented grains, with no evidence of large columnar grains grown along the building direction or cellular solidification substructure. According to Lejček et al. [29], this microstructure is due to the allotropic behaviour of pure iron, which determines solid-state phase transformation and recrystallization during the complex thermal cycles that the metal experiences in the L-PBF process. In fact, pure iron undergoes a phase transition between α-Fe (with body-centred cubic structure, bcc) and γ-Fe (with face-centred cubic structure, fcc) at 912 °C which determines the recrystallization of the microstructure. As a consequence of its peculiar microstructure, pure iron manufactured by L-PBF exhibits a combination of high hardness, tensile strength, and adequate ductility in the as-built condition, which can be possibly exploited for industrial applications [30, 31]. Literature studies [31, 34] investigated the effect of heat treatments on the microstructure and mechanical properties of L-PBF pure iron. On the one hand, Letenneur et al. [31] reported a reduction of tensile strength and an increase in ductility after a stress relieving at 650 °C due to reduction of the dislocation density. On the other hand, Song et al. [34] reported an increase of both tensile strength and ductility after a stress relieving at 640 °C due to grain refinement. Letenneur et al. [31] also investigated the effect of an annealing at higher temperature (1300 °C), reporting that it resulted in a drop in mechanical strength due to the considerable grain growth.

Although several studies addressed the characterization of microstructure and mechanical properties of pure iron manufactured by L-PBF [29–31, 34, 35], the thorough characterization of its magnetic behaviour is not addressed in the existing literature works to the best of authors' knowledge. Instead, different literature studies already addressed the magnetic behaviour of Fe-Si alloys manufactured by L-PBF. Garibaldi et al. [18, 26, 28] reported that the magnetic softness of a Fe-6.9 wt% Si alloy manufactured by L-PBF dramatically improved after an annealing at 1150 °C. However, when the heat treatments performed on pure iron and Fe-Si alloys are compared, it must be considered that, in Fe-Si alloys with Si content higher than about 3, the phase transition between bcc α-ferrite and fcc γ-austenite (which occurs for pure iron at 911 °C) is suppressed and the alloy maintains the bcc structure up to melting. Consequently, Fe-Si alloys can be annealed at high temperatures to promote the desired grain growth for enhancing magnetic softness [17, 18].

Based on the above, the present work aims at: (i) optimizing the L-PBF process of pure iron with the target of obtaining near full density, crack-free components; (ii) characterizing the microstructure in the as-built condition and

after a stress relief heat treatment; (iii) evaluating the effect of building orientation and heat treatment on the mechanical properties; (iv) characterizing the magnetic properties of L-PBF pure iron, both in the as-built and stress relieved conditions. The results will be compared with data available in literature for commercial pure iron manufactured by conventional processes and pure iron and Fe-Si alloys manufactured by L-PBF, aiming to assess whether the pure iron manufactured by L-PBF possesses an adequate trade-off of mechanical strength and magnetic softness for being suitable for magnetic DC applications.

2 Experimental

A commercial pure iron feedstock powder for L-PBF, produced through gas atomization, was supplied by TLS Technik GmbH [36]. Powder morphology was evaluated on free particles using a field emission-scanning electron microscope equipped with a Bruker energy dispersive spectroscope (FESEM-EDS). The particles size distribution was evaluated by performing image analysis on FESEM images of free particles, using the ImageJ opensource software. Particles were classified in terms of Feret diameter, representative of particle size, and aspect ratio (AR), representative of particle shape. Chemical composition and microstructure of the feedstock powder were investigated by FESEM-EDS on mounted, polished and chemically etched (2%vol. HNO_3 in ethanol) cross sections of particles. Phase composition was assessed by X-ray diffraction (XRD) patterns acquired in the 2θ range 30–120 using a Cu-Kα source ($\lambda = 1.5405$ Å) with a step size of 0.02 2θ and a time per step of 3 s. Phase identification was performed using the Pananlytical X'Pert HighScore Plus software.

2.1 Process optimization, sample production and heat treatment

Specimens for the experimental tests were produced using a SISMA/TRUMPF MySint100 L-PBF machine with a cylindrical printing volume (diameter 100 mm, height 100 mm) equipped with a 200 W Trumpf fibre laser source (55 µm spot diameter). The L-PBF process was performed under a nitrogen gas atmosphere with 0.1% residual content of oxygen. To randomize the heat flow during the process, a roto-translating chessboard (3×3 mm^2) scanning strategy was adopted. All the specimens were built using a layer thickness $t = 20$ µm. The *Materialise Autofab* software was used to orient the specimens on the building plate, to create the support structures and to define the process parameters. The feedstock powder was dried at 60 °C for 3 h and sieved before the L-PBF process to prevent particle agglomeration and to improve flowability. To define the optimal set of process parameters, $10 \times 10 \times 15$ mm^3 samples randomly distributed on the building plate were produced, using different combinations of laser power P [W], scan velocity v_{scan} [mm/s] and hatch distance h [µm] (distance between laser tracks). Each combination of process parameters was classified in terms of laser energy density $\text{LED} = \frac{P}{v_{scan} \bullet h \bullet t}$ [J/mm^3], representative of the energy input. Process optimization was performed with the aim of maximizing sample density using the minimum energy input. The optimization procedure was subdivided in two steps, performed at low and high energy input, respectively. In the first step, 32 samples were produced at $P = \{100, 120, 145, 170\}$ W, $v_{scan} = \{500, 700, 900, 1100\}$ mm/s, $h = \{70, 100\}$ µm and $t = 20$ µm, resulting in LED values in the range 46–243 J/mm^3. To investigate the effect of higher energy inputs (up to LED = 405 J/mm^3), a second optimization was performed at $P = 145$, 170 W, $v_{scan} = 300$ mm/s, $h = 70$, 100 µm and $t = 20$ µm. Each combination of parameters (and the corresponding sample) was indicated using the nomenclature "P_v_{scan}_h". The density of each sample was determined by the gravimetric method according to the ASTM B962 standard [37] using an analytical balance (0.0001 g precision). The relative density was calculated respect to the density of pure iron (7.87 g/cm^3) [38]. The set of process parameters "P, v_{scan}, h" which led to a relative density higher than 99% with the lowest LED was chosen as optimal and used for the subsequent manufacturing of specimens for microstructural, mechanical and magnetic characterizations. To further investigate the influence of energy input on the porosity content, the relative density was calculated via image analysis (considering the area fraction of defects) on micrographs acquired using a Zeiss Axio Imager.A1M optical microscope (OM) on mounted and polished cross-sections extractred from samples built at different LEDs. In particular, the 100_900_100 (LED = 56 J/mm^3), 120_900_70 (LED = 95 J/mm^3), 170_500_70 (LED = 243 J/mm^3) and 170_300_70 (LED = 405 J/mm^3) samples were examined. OM images were acquired on both vertical (parallel to the building direction z) and horizontal (parallel to the x–y plane of laser scanning) sections.

Figure 1 summarizes the geometry and orientation on the building plate of specimens for tensile (Fig. 1a–c) and magnetic tests (Fig. 1d–f), respectively. Specimens were manufactured by L-PBF using the optimal set of process parameters previously determined ($P = 170$ W, $v_{scan} = 500$ mm/s, $h = 70$ µm, $t = 20$ µm, as will be shown in Sect. 3). To evaluate the effect of building orientation on the tensile behaviour, both vertical (90°) and horizontal (0°) tensile specimens (consistent with ISO 6892 [39]) were built. 8 tensile specimens for each orientation were produced. Instead, the toroidal samples for magnetic tests (external diameter 80 mm, internal diameter 70 mm, 4 mm height) were

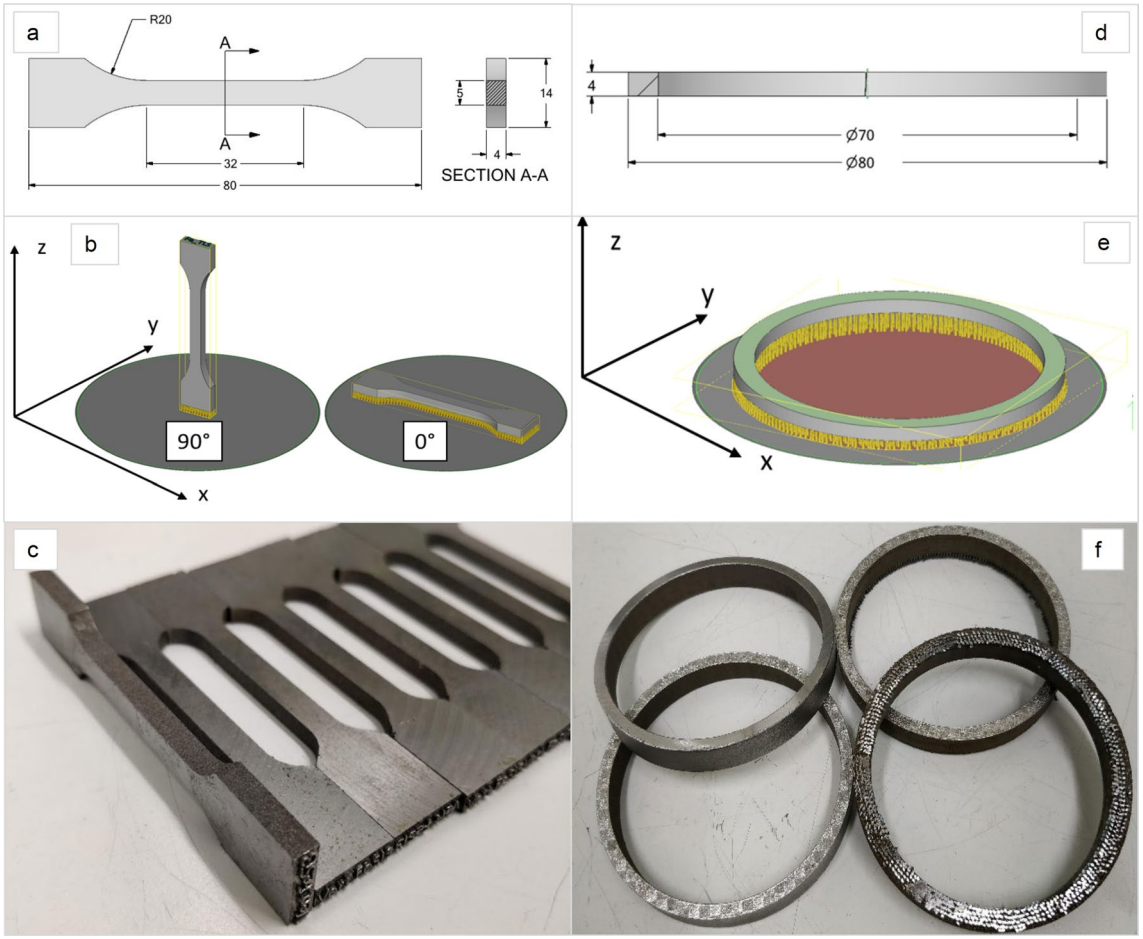

Fig. 1 **a** Specimens for tensile tests (dimensions in mm); **b** schematic representation of the building orientation of vertical (90°) and horizontal (0°) specimens; **c** actual image of specimens; **d** toroidal specimens for magnetic tests (dimensions in mm); **e** representation of their building orientation; **f** actual image of specimens

manufactured by L-PBF with the revolution axis parallel to the vertical building direction. All the specimens were finished by milling to the final dimensions reported in Fig. 1a, d before tensile and magnetic tests, in order to eliminate the regions characterized by high surface roughness and microstructural inhomogeneity near the support region. Actual images of tensile and magnetic specimens used for the tests are reported in Fig. 1c, f, respectively.

To evaluate the effect of a post-process heat treatment, a stress relief anneal at 850 °C for 1 h followed by air cooling was performed. Annealed samples were identified as "HT", in opposition to the L-PBF as-built (AB) ones. The annealing temperature (850 °C) was chosen in the recommended temperature range to achieve optimal magnetic performances in ARMCO® pure iron (816–871 °C, indicated as magnetic anneal) [4]. The performed heat treatment aimed at improving the magnetic performance by relieving the residual stress and reducing the density of dislocations, while avoiding the phase transition from α-Fe to γ-Fe at 911 °C and the consequent recrystallization in order to retain the high mechanical strength resulting from the L-PBF process. In fact, in [31] it was reported that an annealing in the γ-Fe region induced a dramatic drop in the mechanical strength of pure iron manufactured by L-PBF compared to the AB condition and to the material annealed at 650 °C, below the α-Fe to γ-Fe phase transition.

2.2 Microstructural, mechanical and magnetic characterization

Chemical composition of L-PBF samples was checked by means of Glow Discharge Optical Emission Spectroscopy (GDOES, GDA-650, Spectruma Analytik GmbH, Hof, Germany) according to ISO 14707 [40]. Phase identification of AB and HT samples was performed by XRD on vertical cross-sections as previously described in Sect. 2.1. Microstructural analyses were performed by OM and FESEM-EDS on samples extracted from both AB and HT tensile

specimens. Cross-sections for metallographic analyses were prepared by mounting, grinding with abrasive papers up to 1200 grit, polishing with diamond suspension (9 µm, 3 µm, 1 µm) according to ASTM E3 [41] and etched with 2% vol. HNO_3 in ethanol. Hardness, tensile and magnetic tests were performed on the specimens shown in Fig. 1, in both the AB and HT conditions. Stress-controlled tensile tests were performed according to the ISO 6892 standard using a servo-hydraulic machine. The four combinations of building orientation (90°, 0°) and heat treatment (AB, HT) investigated are summarized in Table 1. Four specimens for each combination were tested. The 0.2% proof stress ($R_{p0.2}$), ultimate tensile strength (UTS) and elongation to fracture ($A\%$) were computed from the engineering stress–strain curves, according to ISO 6892. Furthermore, the strain hardening exponent n was evaluated from the true stress-true strain curves according to ISO 10275 [42], aiming to investigate the plastic behaviour of the material. Brinell indentations were performed according to ISO 6506 [43] (2.5 mm sphere, 62.5 kg load) on AB and HT tensile specimens. The fracture surfaces of tensile specimens were investigated by FESEM-EDS to determine the mechanisms of failure.

The magnetic properties were investigated on the toroidal specimens (rings) shown in Fig. 1d, e, f. DC measurements (normal magnetization curves J (H), coercivity H_C and remanent polarization J_r) were carried out through the ballistic method according to the IEC 60,404–4 standard (maximum applied field $H_{max} = 10^4$ A/m). AC measurements were carried out using a Brockhaus C510 electrical steel tester, operating at a minimum excitation frequency of 12 Hz. The samples were tested with sinusoidal excitation at frequency $f = 12$, 20, 30, 40 and 50 Hz, at peak polarization $J_p = 0.5$, 1.0 and 1.5 T. The total energy loss W at given values of f and J_p was expressed in J/kg units by dividing the loop area of the corresponding (J, H) hysteresis loop by the mass density of the sample. In order to investigate the effect of the annealing heat treatment on the magnetic properties, toroidal specimens were tested both in AB and HT conditions.

Table 1 Conditions investigated by tensile tests

Heat treatment	As-built	Heat treated
Orientation		
Vertical	AB_90°	HT_90°
Horizontal	AB_0°	HT_0°

3 Results and discussion

3.1 Feedstock powder

Figure 2 shows the distributions of Feret diameter (Fig. 2a) and aspect ratio (Fig. 2b) for the investigated feedstock powder in the as-received condition. As can be noted, the distribution of Feret diameter can be roughly approximated by a log-normal distribution, i.e., a normal distribution when represented in a semi-logarithmic scale, indicating that the particle size distribution is severely skewed towards little values. This conclusion is supported by the 10th, 50th and 90th percentiles of the distribution, respectively equal to $FD_{10} = 3.5$ µm, $FD_{50} = 8.7$ µm and $FD_{90} = 31.8$ µm. The high fraction of fine particles was confirmed by the FESEM observations of free particles and cross-sections, shown in Fig. 3. The particles composing the feedstock powder exhibited a regular and spherical morphology, as suggested by the aspect ratio distribution (Fig. 2b) and visible in the FESEM

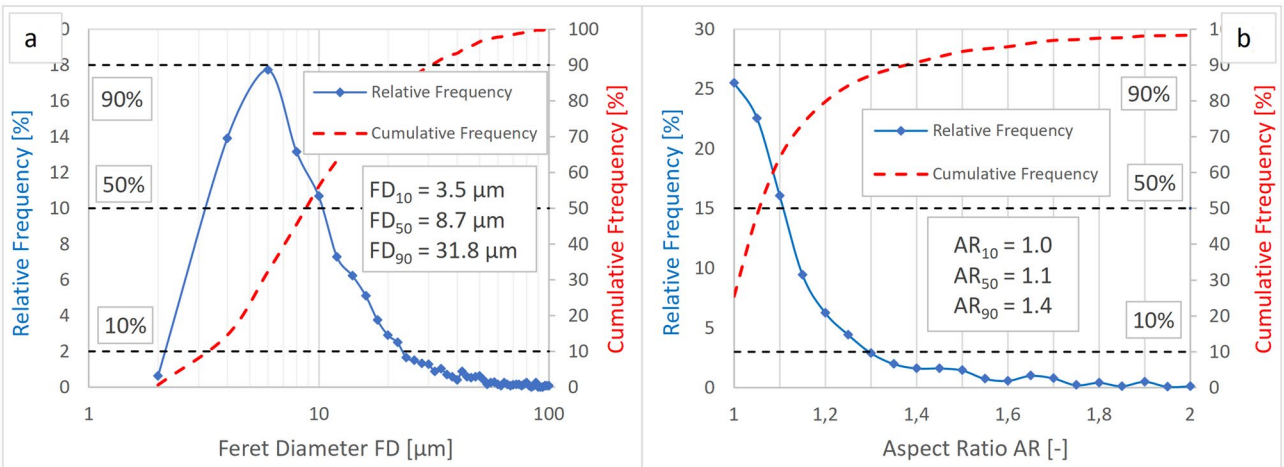

Fig. 2 Particle size distributions of Feret diameter (**a**) and aspect ratio (**b**) for the investigated feedstock powder. Note that the distribution of Feret diameter in (**a**) is plotted in a semi-logarithmic scale

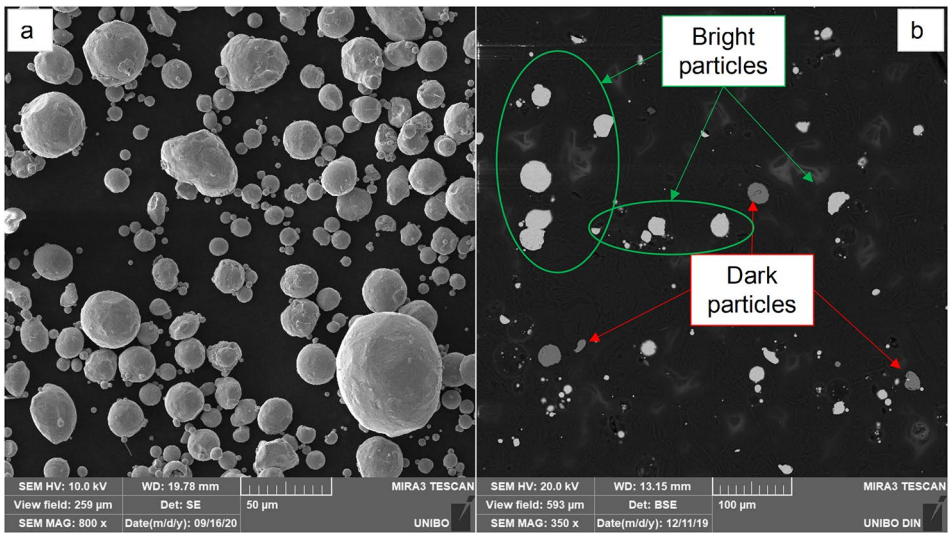

Fig. 3 FESEM images of **a** free particles, **b** mounted and polished particles

images in Fig. 3. Few particles with irregular, elongated morphology, as well as satellites, were identified. According to the distribution in Fig. 2b, the 50% of particles were characterised by an AR ≤ 1.1 (AR_{50}), while only the 10% exhibited an AR ≥ 1.4 (AR_{90}). Near the totality of observed particles lied in a range of AR between 1.0 (perfectly spherical particle) and 2.0 (ellipsoidal particles with the major axis double the length of the minor), suggesting an overall high degree of sphericity of the feedstock powder. This evidence is consistent with the gas atomization process by means of which the investigated powder was produced, which usually leads to spherical particles with a regular surface [44].

FESEM observations in back-scattered electrons imaging (BSE) of mounted and polished particles (Fig. 3b) revealed the presence of two distinct types of particles with different brightness, thus different chemical composition. The semi-quantitative chemical composition of particles reported in Table 2, assessed through FESEM-EDS, confirmed this finding. The largest fraction of particles exhibited the brightest appearance and were mostly composed of Fe with traces of Mn. Instead, darkest particles (which represented a little fraction of the total number of particles, in comparison to brightest ones) showed a high content of Al and O beside Fe, with low amounts of Si, Zr, Mn and Ti. Due to the high content of Al and O in conjunction with Si, Ti and Zr, darkest particles appeared consistent with non-metallic inclusions, possibly resulting from the manufacturing process of the powder. Note that the C content reported in Table 2 is likely to come from the mounting media.

Microstructure of the feedstock powder appeared composed of fine polygonal grains, with no evidence of dendritic or cellular solidification structures (Fig. 4a), consistently with the solidification structure of pure metals [45], as previously described by Lejček et al. [29, 35]. High magnification FESEM observations in Fig. 4b revealed the presence of sub-micron spherical particles dispersed within the microstructure. However, XRD analyses only indicated the presence of α-Fe (PDF number 006-0696) in the feedstock powder, as visible in Fig. 5a (black line). No other diffraction peaks associated to crystalline phases were detected beside α-Fe. It is possible that the particles in Fig. 4b are present in a volume fraction lower than the detection limit of XRD or, conversely, that they possess no crystalline structure (amorphous phases) resulting in no diffraction peak. Song et al. [30] and Lejček et al. [35] reported the presence of similar particles in pure iron manufactured by L-PBF, indicating that they are complex oxides containing Fe, Cr, Sn and Si [35] or Cr, Mn and V [30]. However, while Song et al. [30] proposed that particles formation occurs during the L-PBF process, Lejček et al. [35] suggested that the particles observed in L-PBF samples were already present in the feedstock powder, consistently with the evidence shown in the present work in Fig. 4b.

3.2 L-PBF process optimization

Figure 6 reports the trend of relative density measured on L-PBF samples against the energy input LED. Each point

Table 2 Semi-quantitative chemical composition of particles observed in Fig. 3b evaluated by FESEM-EDS

Wt%	Fe	Mn	O	Al	Si	Ti	Zr	C
Brightest particles	87.9	1.4	1.2	–	–	–	–	9.5
Darkest particles	20.1	1.1	43.8	23.6	2.3	0.8	1.5	6.8

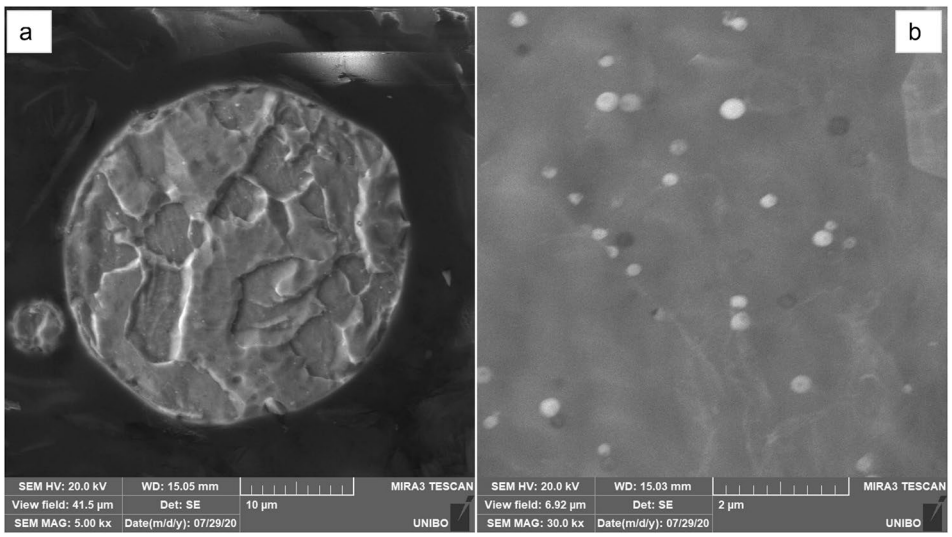

Fig. 4 FESEM images showing the microstructure of the feedstock powder (**a**) and the sub-micron spherical particles at higher magnification (**b**)

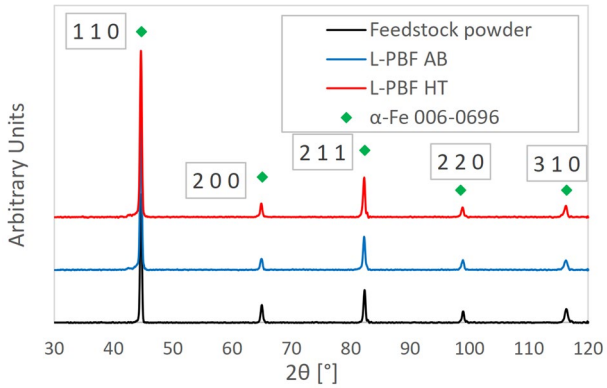

Fig. 5 X-ray diffraction patterns of the feedstock powder (in black) and L-PBF samples in the as-built (AB) and annealed (HT) conditions

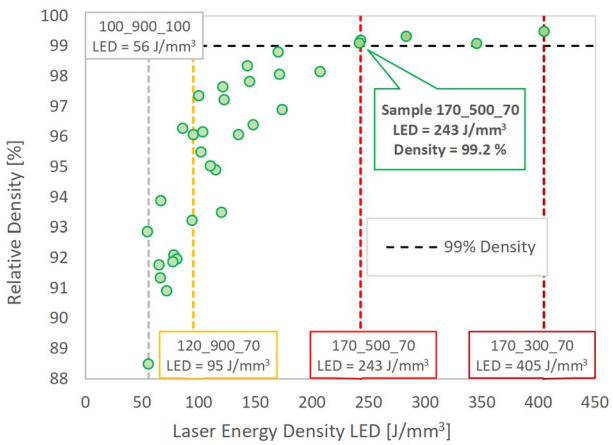

Fig. 6 Plot of the relative density [%] against the energy input LED [J/mm^3] for each combination of process parameters. The dashed vertical lines indicate the samples furtherly investigated by OM

represents a set of process parameters "P, v_{scan}, h". As can be seen, a good correlation between energy input LED and sample density was found. As reported in Sect. 2, the target for process optimization was the maximizazion of the material density with the minimum energy input. Hence, the set of process parameters "$P = 170$ W, $v_{scan} = 500$ mm/s, $h = 70$ µm and $t = 20$ µm" (briefly indicated as "170_500_70"), was chosen as the optimal set of process parameters, since it resulted in a relative density of 99.2% with a LED = 243 J/mm^3.

As can be noted, the LED-density trend can be subdivided in two distinct regions. At relatively low energy inputs (LED < 200 J/mm^3), the density increases with the energy input. This trend is mantained until the relative density approaches 99%. Note that in this region, several LED-density points exhibited a very different density for extremely similar LED (obtained using different combinations of process parameters P, v_{scan}, h), thus resulting in a great scatter of the LED-density trend. For LED > 200 J/mm^3, the LED-density trend saturates, since the density remains approximatively constant (between 99 and 99.5%) over a wide range of energy input. Figure 7a reports the OM images acquired on vertical polished cross-sections. As can be noted, samples produced at low LED (100_900_100, LED = 56 J/mm^3 and 120_900_70, LED = 95 J/mm^3) exhibited a great number of large and irregular defects, consistent with the typical morfology of lack of fusion (LoF) defects, whose formation is due to an insufficient energy input for the proper melting of the powder layer [10]. Therefore, it can be assumed that in the low energy input regime, a LED increase involves a higher energy available for the melting of the feedstock powder, leading to less lack of fusion defects and thus higher density. In contrast, samples produced at high LED (170_500_70, LED = 243 J/mm^3 and 170_300_70,

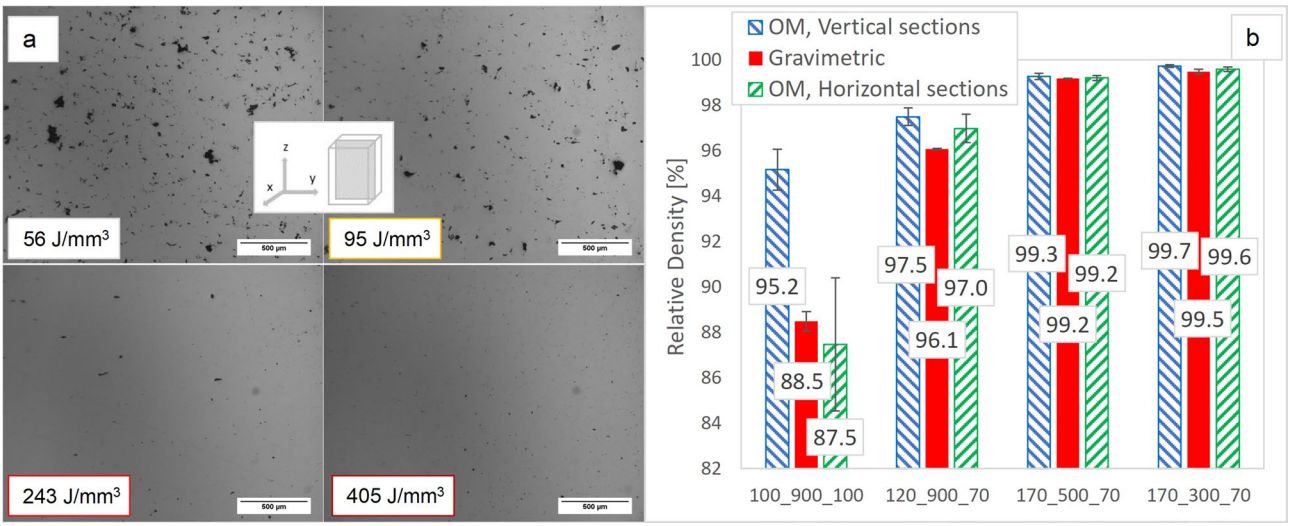

Fig. 7 OM images of vertical sections (polished and unetched) of samples produced at different LED: 100_900_100 (56 J/mm^3), 120_900_70 (95 J/mm^3), 170_500_70 (243 J/mm^3) and 170_300_70 (405 J/mm^3) (**a**). Comparison between the relative density of the same samples evaluated by OM on vertical and horizontal sections and by the gravimetric method. T-bars indicate the standard deviation (**b**)

LED = 405 J/mm^3) exhibited a little number of small and regular defects. Some elongated defects are still visible in the 170_500_70 sample, while in the 170_300_70 sample all the detected defects show a circular morfology (on the considered 2-D section) and no lack of fusion defects are visible. Hence, it can be concluded that for LED > 200 J/mm^3 the energy input is sufficient to completely melt the pure iron feedstock powder. However, the detection of small and regular defects, consistent with the morphology of gas pores indicates that the formation of defects can also occurr in samples prepared at LED > 200 J/mm^3 (up to 400 J/mm^3), thus hindering the manufacturing of full-density specimens even at very high energy input. Spherical gas pores typically originate from gas porosity inside the feedstock powder or from the entrapping of inert gas from the working chamber due to melt pool flow or keyhole formation [10, 11].

Figure 7b compares the relative density measured by the gravimetric method and image analysis on both vertical and horizontal sections for the four aforementioned samples. As can be noted, in case of samples characterized by high LED and density, no appreciable differences between gravimetric and image analysis densities (evaluated on both vertical and horizontal sections) were found. On the other hand, these values strongly differ in low LED, low density samples, in particular in the 100_900_100 sample. A possible explanation is the morphology of the existing defects. For high LED, defects are nearly spherical pores, hence their area does not depend on the considered section plane. Instead, the lack of fusion defects detected in low LED samples have an irregular morphology, which results in different areas on vertical and horizontal section planes.

3.3 Microstructure of L-PBF specimens

Table 3 reports the chemical composition of L-PBF samples evaluated by GD-OES. As can be noted, a Fe content of 99.848 wt% was measured, confirming the high purity of the samples manufactured by L-PBF. The major impurity found was Al, followed by Mn. Compared to the ARMCO® pure iron grade 4 [4], the material studied in the present work possess an extremely similar Fe and impurity content. Considering the high purity of L-PBF samples, it appears plausible that the amount of dark particles visible in Fig. 3b could be not representative of their actual amount in the feedstock powder and mislead to an overestimation of the impurities content in the feedstock powder. Since the available equipment did not allow the precise evaluation of the chemical composition of the feedstock powder, the high purity level shown by Table 3, evaluated on L-PBF samples, was also considered representative of the initial feedstock powder.

OM images of the AB microstructure of L-PBF specimens are shown in Fig. 8a, b. The microstructure was

Table 3 Chemical composition (wt%) of L-PBF specimens evaluated by GD-OES

Element	Fe	C	Al	Mn	P	S
(wt%)	99.848	0.001	0.047	0.011	0.0051	0.0032

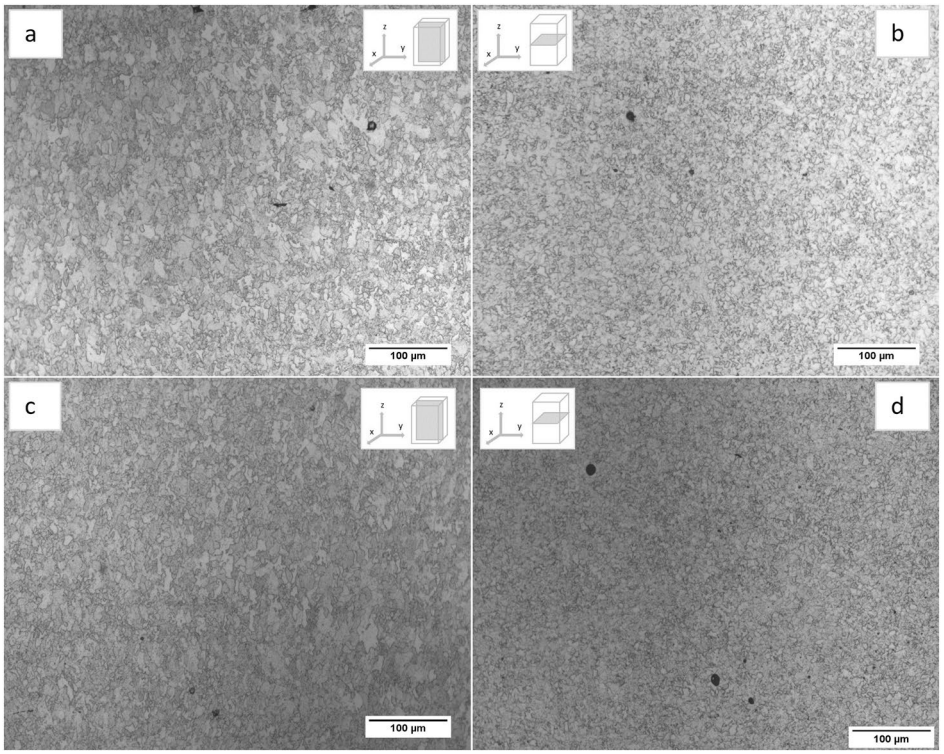

Fig. 8 OM images of the microstructure of pure iron L-PBF samples in the as-built (AB; **a**, **b**) and annealed (HT; **c**, **d**) conditions, along vertical (**a**, **c**) and horizontal (**b**, **d**) cross-sections

composed of fine, nearly equiaxed grains, with an average size of ≈ 5 µm (consistent with ASTM grain size number 12 according to ASTM E112-13 [46]). No difference between the microstructure on vertical (Fig. 8a) and horizontal (Fig. 8b) cross-sections was noted. The AB microstructure of L-PBF pure iron did not exhibit the typical features of metallic L-PBF components, as already reported in the literature [29–32]. No melt pool and scan track borders or columnar grains oriented along the building direction, typically observed in alloys processed by L-PBF, were observed. Furthermore, no solidification substructure was observed at higher magnification, as clearly visible in the FESEM images in Fig. 9.

Due to the extremely low impurities content (≈ 0.15 wt% according to GD-OES analyses reported in Table 3), the investigated material can be considered as pure iron. Hence, the absence of a cellular solidification structure, generally observed in alloys processed by L-PBF, can be explained by the typical solidification mechanism of pure metals. In fact, the solidification of non-planar structures

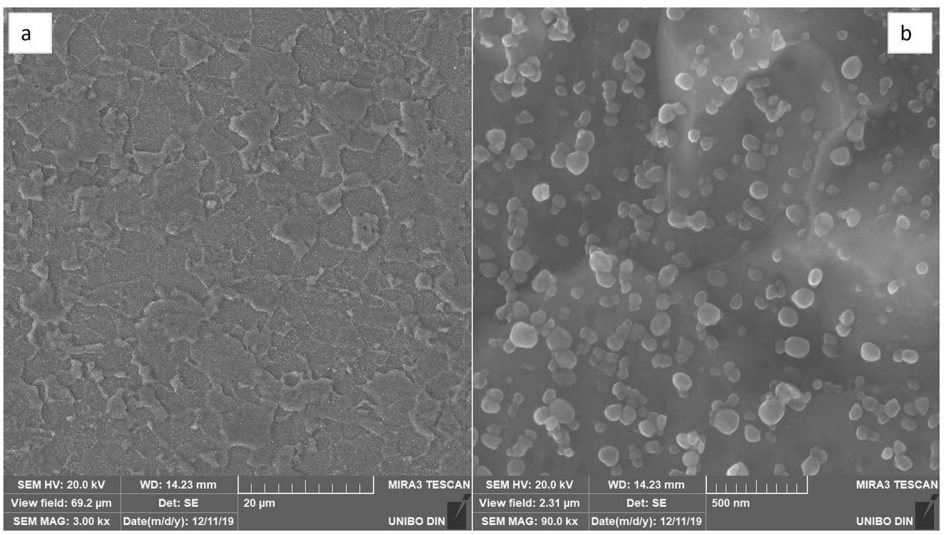

Fig. 9 FESEM images of the as-built (AB) microstructure: grain structure (**a**) and sub-micron spherical particles (**b**)

(cellular, columnar and equiaxed dendritic structures) requires a sufficient amount of undercooling, which, in case of alloys, is provided by micro-segregation of alloying elements (constitutional undercooling). However, no constitutional undercooling is possible for pure metals due to the absence of solute segregation. For a pure metal, the solidification in non-planar structures can take place only if the melt is thermally undercooled. As a result, pure metals often solidify in planar structures, thus forming columnar, oriented grains [45, 47]. Moreover, the solidification in the L-PBF process, similarly to welding, is characterized by high melt superheating and temperature gradients, which further promote the solidification of planar structures [48]. Following these considerations, it would be expected for pure iron manufactured by L-PBF an as-built microstructure composed of columnar oriented grains. Instead, the OM images in Fig. 8a, b indicated an AB structure composed of fine, non-oriented grains. A similar result was found by Lejček et al. [29], who proposed a model for the explanation of this microstructure based on the allotropic behaviour of iron. According to Lejček et al. [29], the L-PBF solidification of pure iron occurs through the formation of primary α-Fe columnar grains from the melt pool border oriented toward the melt pool centre. Then, the thermal cycles resulting from the processing of subsequent layers determine the α-Fe → γ-Fe → α-Fe phase transformation of the previously solidified metal and the consequent breakdown of primary columnar grains. Following this model, the observed as-built microstructure can be considered as originated by an in-situ recrystallization of the primary solidification structure occurring during the thermal cycles typical of the L-PBF process. A further possible support to the explanation provided by Lejček et al. in [29] can be found considering Fe-Si alloys with high Si manufactured by L-PBF. In fact, Garibaldi et al. [17] showed that the as-built microstructure of a Fe-Si alloy with 6.9 wt% of Si is composed of large columnar grains, highly oriented along the building direction. Noticeably, Fe-Si alloys with a similar Si content do not possess any α-Fe → γ-Fe transition, hence no phase transition (and consequent recrystallization) is expected during their L-PBF process. FESEM observations at higher magnifications (Fig. 9a) confirmed the grain morphology previously described and the absence of a cellular substructure. Furthermore, a dense distribution of small spherical particles, similar to those observed in the feedstock powder but with lower size (< 100 nm) and in a higher volume fraction, was observed (Fig. 9b). The assessment of the chemical composition of these fine particles by FESEM-EDS was not possible due to their very small size. Song et al. [30], and Lejček et al. [35] reported the presence of similar particles in pure iron manufactured by L-PBF, ascribing their origin to Cr, Mn and V rich impurities. Different authors [49–51] reported the presence of nano-inclusions with similar morphology containing O and elements with a high affinity with it (mainly Si and Cr) in the microstructure of the AISI 316L stainless steel processed by L-PBF. These particles were identified as amorphous silicates (also containing Mn and Cr) resulting from the reaction between Si and O pick-up from the working chamber, which formation is promoted by the extremely high cooling rates of L-PBF. As reported in Table 3, the major impurity detected in the present work in L-PBF pure iron was Al, which is characterized by a high affinity with O. Even though it was not possible to establish the chemical composition of the observed particles, it can be supposed that they are oxides originating from the impurities present in the feedstock powder, similarly to what reported in [30, 35].

Figure 8c, d show the microstructure after stress relief annealing (HT condition). From the comparison with Fig. 8a, b, no appreciable modification in terms of grain size and morphology resulting from the annealing can be observed. This evidence is consistent with the annealing temperature (850 °C), lower than the α-Fe → γ-Fe transition temperature of pure iron (912 °C [38]), hence no recrystallization of the as-built structure is expected. The XRD patterns in Fig. 5 indicated α-Fe (PDF number 006-0696) as the only crystalline phase present in both AB and HT specimens, as for the feedstock powder.

3.4 Hardness and tensile properties

Representative stress–strain curves for the various building orientations and heat treatment conditions investigated are reported in Fig. 10. Table 4 summarizes the values of hardness, tensile properties $R_{P0.2}$, UTS and A% and strain hardening exponent n calculated from stress–strain curves. For comparison, Table 4 also reports the corresponding values for L-PBF manufactured pure iron from previous literature studies [31, 34, 35] and the ones declared by the producer for

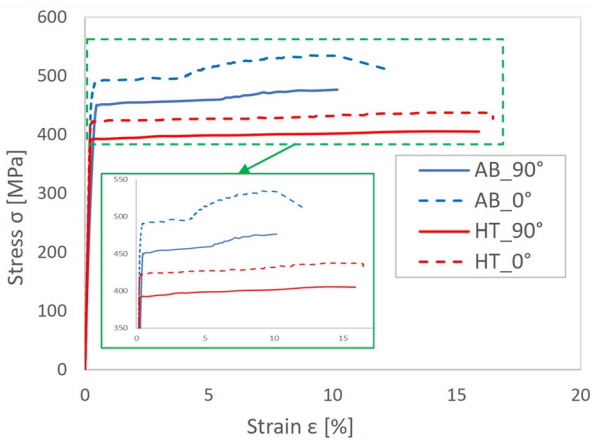

Fig. 10 Representative stress–strain curves obtained from tensile tests

Table 4 Summary of results of tensile tests ($R_{P0.2}$, UTS, $A\%$, n) and hardness measurements performed in the present work in the as-built (AB) and annealed (HT) conditions, compared to results from previous literature studies on L-PBF pure iron [31, 34, 35] and conventionally manufactured ARMCO® pure iron [4]

Condition	$R_{P0.2}$ [MPa]	UTS [MPa]	$A\%$ [%]	n [–]	HB
AB_90° (this work)	455 ± 6	477 ± 2	10.0 ± 0.6	0.13 ± 0.01	177 ± 3
AB_0° (this work)	484 ± 6	530 ± 6	12.0 ± 0.7	0.14 ± 0.00	
HT_90° (this work)	399 ± 6	407 ± 7	15.0 ± 1.4	0.10 ± 0.01	149 ± 3
HT_0° (this work)	423 ± 6	439 ± 1	15.9 ± 0.5	0.10 ± 0.02	
L-PBF pure iron, as-built (90°) [31]	450 ± 3	500 ± 4	13.7 ± 0.8	–	–
L-PBF pure iron, as-built (0°) [31]	554 ± 5	599 ± 9	13.7 ± 0.8	–	–
L-PBF pure iron, as-built (90°) [35]	356 ± 2	435 ± 2	18 ± 1	–	157 ± 4 HV
L-PBF pure iron, as-built (0°) [35]	369 ± 2	433 ± 2	23 ± 1	–	159 ± 4 HV
L-PBF pure iron, as-built [34]	256 ± 17	357 ± 22	9.1	–	–
L-PBF pure iron, 640 °C for 2.5 h [34]	352 ± 21	410 ± 23	14.6	–	–
L-PBF pure iron, 650 °C for 30 min (0°) [31]	–	500	18	–	–
L-PBF pure iron, 1300 °C for 2 h [31]	210	330	30	–	–
ARMCO® pure iron (annealed at 650–950 °C) [4]	186	290	38	–	74–83
ARMCO® pure iron (annealed at ≈ 1200 °C) [4]	138	276	40	–	30–40 HRB

the ARMCO® pure iron, annealed between 650 and 950 °C (heat treatments indicated by the producer as stress relief, magnetic and recrystallization anneals) and at 1200 °C (indicated by the producer as high temperature anneal) [4]. The tensile properties measured in the present work for pure iron L-PBF appeared comparable to those reported in literature in [31, 34, 35], for both AB and HT specimens. In all the investigated conditions, tensile strength and ductility resulted respectively higher and lower than the reference values for pure iron ($R_{P0.2}$ = 98–166 MPa, UTS = 158–225 MPa [30], UTS = 305–360 MPa and $A\%$ = 32–48% [31]). Tensile strength and hardness also resulted considerably higher than those reported for ARMCO® pure iron subjected to both stress relief, magnetic, recrystallization or high temperature anneal in [4]. Therefore, it can be concluded that pure iron manufactured by L-PBF exhibited a considerably higher strength than the conventionally manufactured one, especially in the AB conditions. Song et al. [30] and Lejček et al. [35] proposed that the high strength of pure iron manufactured via L-PBF originated from three different contributions, which are (i) grain refinement, (ii) high density of dislocations (indicated as work hardening in [30]) and (iii) precipitation strengthening by oxide particles. As described by Lejček et al. in [29] and previously reported in Sect. 3.3, the fine-grained microstructure, responsible of the (i) contribution, arises from the recrystallization during the L-PBF process of the primary solidification structure due to the combination of allotropic behaviour of pure iron and the complex thermal cycles during the L-PBF process. Lejček et al. [29] reported a very high density of dislocations in pure iron manufactured by L-PBF in the as-built condition (in the order of 10^{14} m^{-2}), which contributes to the strengthening by the (ii) term, attributed to the extremely high cooling rates (10^4–10^6 K/s [10]) experienced by the metal during the L-PBF solidification [29]. Letenneur et al. and Lejček et al. [29, 31] also indicated that, due to these high cooling rates, formation of martensite upon solidification is also possible, despite the extremely low carbon content. The martensitic transformation could represent an additional source of dislocations, thus supporting the overall strengthening by (ii) contribution. According to Song et al. [30], the precipitation strengthening due to the sub-micron oxide particles (iii) (contribution) is negligible.

The mechanical properties appeared significantly affected by heat treatment condition and build orientation. Considering the effect of the heat treatment, the performed annealing at 850 °C for 1 h induced a reduction of hardness and tensile strength and a ductility increase, as indicated by the higher hardness, $R_{p0.2}$ and UTS and lower $A\%$ in the AB condition than HT condition, similarly to the results reported in [31]. On the opposite, Song et al. [34] reported an increase of both tensile strength and ductility after a stress relieving at 640 °C for 2.5 h, ascribing it to the reduction of dislocations and grain refinement due to recrystallization occurring during the heat treatment. In the present work, no recrystallization due to the annealing was observed, as shown in Fig. 8. Considering the effect of the performed annealing on the mechanical properties, the absence of differences in the grain structure and size between AB and HT samples shown in Fig. 8 and previous literature works [30, 31, 35], it can be reasonably inferred that (a) the higher hardness, $R_{p0.2}$ and UTS of as-built L-PBF manufactured pure iron than the conventionally manufactured one are probably mainly due to the fine-grained microstructure and the high density

of dislocations resulting from the solidification conditions and recrystallization during the L-PBF process and (b) the reduction of hardness, $R_{p0.2}$ and UTS and the A% increase in the HT condition compared to the AB probably result from the reduction of the dislocations density due to the annealing, thus the reduction of (ii) strengthening contribution. The different plastic behaviour exhibited by AB and HT specimens during tensile tests (visible in Fig. 10 and quantified by the strain hardening exponent n in Table 4) possibly supports these assumptions. In fact, while AB specimens showed a certain amount of strain hardening during tensile tests, starting from an engineering strain of 4–5%, HT specimens exhibited a nearly ideal plastic behaviour during the plastic flow with extremely low strain hardening. At the same time, the strain hardening exponent n decreased from 0.13 to 0.14 in the AB condition to 0.10 after annealing (HT condition), thus quantifying the lower strain hardening after annealing treatment. It is know that strain hardening occurs due to the interaction of dislocations during plastic flow [52]. While Lejček et al. [29] measured a very high density of dislocations in pure iron manufactured by L-PBF in the as-built condition, as previously reported, Song et al. [34] estimated a reduction of the lattice microstrain (which is related to the density of lattice defects) from XRD analyses of approximatively one order of magnitude in pure iron manufactured by L-PBF after an annealing treatment at 640 °C. Following these considerations, the higher strain hardening in the AB condition possibly appears consistent with the high dislocation density due to the L-PBF process demonstrated by Lejček et al. [29], while the lower strain hardening in the HT condition can indicate a lower density of dislocations.

Considering the effect of the building orientation, Table 4 shows a mild anisotropy in the tensile properties, characterized by higher $R_{p0.2}$, UTS and $A\%$ along the horizontal direction (0° specimens). The same anisotropy was reported by Letenneur et al. in [31]. In the present work, the tensile anisotropy was quantified through an anisotropy index I_P, defined as $I_P = \frac{P_{0°} - P_{90°}}{P_{0°}}$, where P indicates the considered mechanical property for vertical (90°) and horizontal (0°) specimens. A high I_P indicates a high anisotropy of the considered property P between 0° and 90° specimens. The values of I_P calculated for $R_{P0.2}$, UTS and $A\%$ are summarized in Table 5. As can be noted, the annealing treatment mainly reduced the anisotropy of $A\%$ and, in a less extent, of UTS, while it did not affect the anisotropy of $R_{P0.2}$. L-PBF components often shows an anisotropic tensile behaviour, exhibiting lower tensile strength and ductility along the vertical direction. A first contribution to this behaviour comes from defects. In particular, lack of fusion defects generally possess an irregular morphology and are roughly parallel to the horizontal plane of laser scanning. Hence, in vertical specimens (90°), lack of fusion defects are normal to the load direction, while they are parallel in horizontal specimens (0°) [10]. As a result, their effect on the tensile properties is more pronounced in 90° specimens than 0° ones, thus leading to higher $R_{P0.2}$, UTS and $A\%$ for 0° specimens. However, the morphology of L-PBF defects is not affected by the annealing treatment, hence it would be expected for the tensile anisotropy not to change between AB and HT specimens. Instead, Table 5 clearly shows a reduction of the anisotropy for UTS and $A\%$. According to [31], this anisotropy can arise from the residual stress originated during the L-PBF process, which possess a different intensity on vertical and horizontal planes [53]. Since the performed anneal induced a stress relief, as demonstrated in [34], it is possible that the reduced anisotropy for HT specimens comes from the relief of residual stresses.

Table 5 Anisotropy index for $R_{P0.2}$, UTS and $A\%$ calculated for as-built (AB) and annealed (HT) specimens

Anisotropy index $I_P = \frac{P_{0°} - P_{90°}}{P_{0°}}$ [–]	AB	HT
$R_{P0.2}$	0.06	0.06
UTS	0.10	0.03
$A\%$	0.17	0.05

Representative fracture surfaces of the tensile specimens, reported in Fig. 11, show micron and sub-micron sized dimples, observed in all the investigated conditions, with no evidence of cleavage or intergranular brittle failure, thus confirming the ductile behaviour indicated by tensile tests. Small, spherical particles were observed inside the dimples, with a size consistent with the very fine particles shown in Fig. 9. The same fracture morphology was observed for both AB and HT specimens, but with larger dimples in the case of HT specimens.

3.5 Magnetic properties

Figure 12a shows the normal DC magnetization curves J (H) measured on the AB and HT toroidal samples. The corresponding curves of relative permeability μ_r (defined as $\mu_r = 1 + J/\mu_0 H$ where μ_0 = magnetic permeability of free space) as a function of H are displayed in Fig. 12b. The magnetic polarization J at H_{max}, indicated as J_{max}, the relative permeability at $H = 100$ A/m, μ_{100} (considered as the initial permeability), the highest measured value of relative permeability μ_{max}, the coercivity H_C and the remanent polarization J_r are reported in Table 6, for both AB and HT toroidal samples. In both samples, J_{max} was equal to ~ 1.8 T, a remarkably high value corresponding to ~ 0.8 J_S, being J_S the saturation polarization of iron (2.15 T at room temperature [1, 2]). This is consistent with the good level of purity and the high density of the L-PBF samples, as previously reported. In the field range 0–400 A/m, the magnetization curve of the AB ring appears almost flat

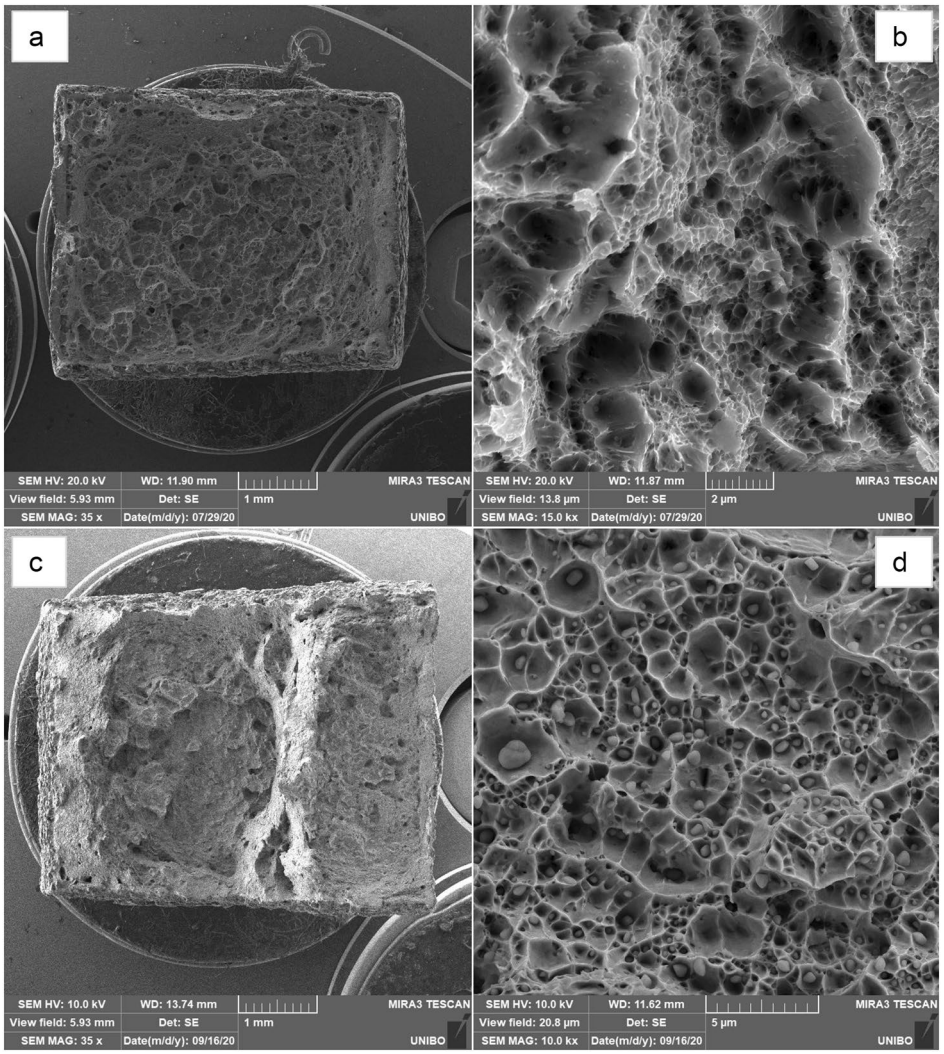

Fig. 11 Representative SEM images of tensile fracture surfaces of L-PBF pure iron in the as-built (AB; **a**, **b**) and annealed (HT; **c**, **d**) conditions. Note the different magnification of **b** and **d**

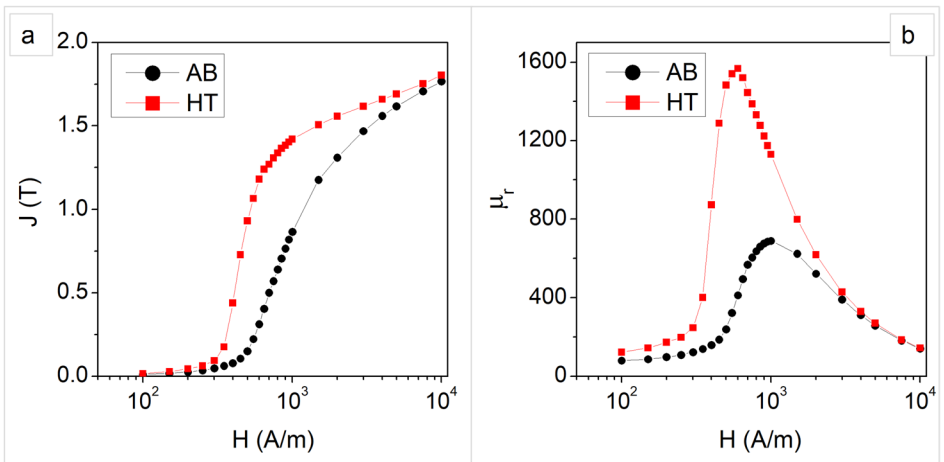

Fig. 12 Normal DC magnetization curves (**a**) and relative permeability μ_r (**b**) of the as-built (AB) and annealed (HT) samples

(Fig. 12a); a similar feature is also visible in the curve of the HT ring even if over a shorter field interval. This is indicative of a domain wall pinning mechanism, which is usually caused by structural imperfections, grain boundaries, precipitates and, in case of magnetostrictive materials, residual stresses. This effect is also responsible for

Table 6 DC magnetic parameters measured on as-built (AB) and annealed (HT) samples (for all values, the experimental error is 2%)

Sample	J_{max} [T]	μ_{100}	μ_{max}	H_c [A/m]	J_r [T]
AB	1.77	79	690	610	1.06
HT	1.80	123	1570	425	1.51

the measured H_C and μ_{max}, which are at least one order of magnitude higher and smaller, respectively, than those typical of iron samples with good magnetic softness [54, 55]. As previously shown, in the investigated samples the average grain size is ≈ 5 µm, a rather small value that implies a high density of grain boundaries. Moreover, the magnetostriction constants of iron are of the order of 10^{-5} [56], which means that internal stresses also play an effective role in hindering the displacement of the domain walls. Compared to the AB ring, the HT one exhibits smaller H_C and higher μ_{100} and μ_{max}. In particular, after the anneal, H_C decreased by about 30% and μ_{max} was more than doubled (Table 6). These differences can be reasonably ascribed to the relief of the residual stresses, generally associated with a reduction of crystal defects, particularly dislocations. The stress relief can also result in an improved squareness of the hysteresis loops of soft magnetic materials [57], which accounts for the considerably higher J_r measured in HT compared to that of AB. In high-purity iron the coercivity decreases with increasing the grain size and H_C ≈ 40 A/m, i.e. one order of magnitude smaller than that measured in sample HT in the present work, is obtained for values of the grain size around 100 µm [58]. Moreover, the highest relative permeability μ_{max} for ARMCO® pure iron ranges between 10^3 and 2×10^4 according to the annealing condition [4], thus up to one order of magnitude higher than the highest μ_{max} measured in the present work on the HT sample. Considering a Fe-6.9 wt% Si alloy manufactured by L-PBF, Garibaldi et al. [18] reported a maximum permeability μ_{max} of 2×10^3 in the as-built condition and higher than 2.4×10^4 after annealing at 1150 °C, while H_c decreased from approximatively 100 to 16 A/m. Therefore, Garibaldi et al. obtained significantly better soft magnetic properties than those of the investigated AB and HT pure iron samples. This is not only to be ascribed to the presence of Si, which reduces the magnetostriction and the magnetocrystalline anisotropy of Fe [59], but also to the microstructural characteristics of the L-PFB Fe-6.9 wt% Si alloy, in particular the presence of a beneficial crystallographic texture and of grains whose size increased from 10-30 µm up to ~ 300 µm after annealing [18]. To summarize, it can be reasonably assumed that the fine-grained structure of the investigated samples remains an issue for the improvement of magnetic softness of pure iron manufactured by L-PBF for prospective DC applications, even after the application of a stress relief annealing.

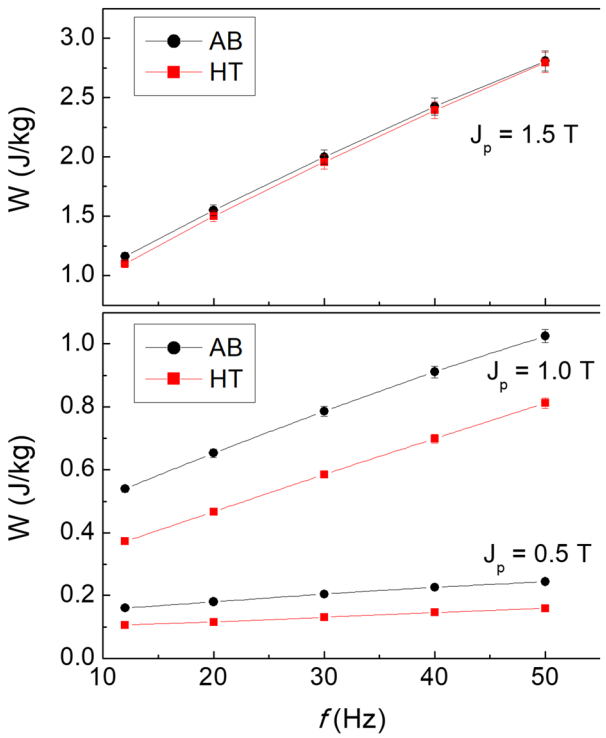

Fig. 13 Energy loss per cycle W vs. magnetizing frequency f in as-built (AB) and annealed (HT) samples at different values of peak polarization J_p. In some cases, the error bar is comparable to the symbol size

The analysis of the AC magnetic properties provided further information on the effect of the heat treatment on the microstructure of the rings. In Fig. 13, the loss parameter W is shown as a function of f. For $J_p = 0.5$ and 1.0 T, the curve of sample HT lies below that of AB and the two curves are almost parallel, which suggests that the hysteresis loss component, i.e., the energy dissipated in the limit $f \to 0$, reduced after annealing, whereas the dynamic loss was not substantially affected. Instead, the curves measured at the highest value of J_p (1.5 T) appear superposed. Hence, it can be inferred that, at this J_p, also the hysteresis loss is similar for AB and HT. This is consistent with the observation that, under the adopted DC measurement conditions, the parameter $4J_rH_C$, which is a rough estimate of the hysteresis loop area [58], is similar for AB and HT samples and its value is ~ 0.33 J/kg.

The dynamic loss component is associated to the eddy currents and is usually separated in two contributions known as classical and excess loss, respectively [54]. The first depends on the sample geometry and is inversely proportional to the electrical resistivity; the second arises from the eddy currents produced by the displacement of the domain

walls and increases with the domain size, as well as with the grain size [54, 60]. In principle, both the classical and excess losses may increase after subjecting an iron sample to annealing treatments, unlike the hysteresis loss. Therefore, at given values of f and J_p, the total loss may be larger or smaller in the HT sample with respect to the AB one, depending on the balance between the different loss contributions [18, 61]. In the case of the AB and HT rings and under the adopted AC measurement conditions, the dynamic loss component does not seem to change, which is consistent with the fact that both samples consist of small grains of similar size. In a pure iron ring produced by L-PBF with dimensions comparable to the samples in the present work, Goll et al. [26] measured a dynamic loss of ~ 0.72 J/kg at $J_p = 1.0$ T and $f = 50$ Hz, which appears consistent with the total loss value found in the HT sample in the present work (~ 0.81 J/kg, Fig. 13).

Considering Fe-4 wt% Si rings produced by L-PBF, Tiismus et al. [61] measured significantly high dynamic losses. In particular, in the as-built Fe-Si ring a total loss of 0.28 J/kg was found at $J_p = 1.0$ T and $f = 50$ Hz, which decreased down to ~ 0.16 J/kg after annealing at high temperature (1150 °C), so as to induce the growth of the grains. The dynamic losses contributed for ~ 74% in the as-built sample and for ~ 88% in the annealed one and were associated to eddy currents generated due to the unlaminated, fully dense cross section of the rings. The dynamic losses were seen to further increase at high magnetic saturation of the material (i.e. by testing the samples at $J_p = 1.5$ T), which was ascribed to the appearance of a nonlinear saturation loss component. In particular, at $J_p = 1.5$ T and $f = 50$ Hz, a total loss of ~ 1.7 J/kg was measured in the annealed Fe-Si ring, being the hysteresis contribution ~ 0.06 J/kg and the dynamic one ~ 1.6 J/kg (i.e., ~ 94% of the total value). In the case of the pure iron samples investigated in the present work, the total loss measured at the same values of peak polarization and frequency (i.e., 1.5 T and 50 Hz, respectively) is ~ 2.8 J/kg both in AB and HT samples (Fig. 13). We can roughly calculate the dynamic loss component by subtracting from this value the quantity 0.33 J/kg (indicated above as a reasonable estimate of the hysteresis loss component at the considered J_p) thus obtaining ~ 2.5 J/kg (~ 89% of the total value). Therefore, the dynamic loss component measured by Tiismus et al. in the Fe-Si ring was, in absolute value, only ~ 40% lower than that estimated for our samples.

Indeed, the results by Tiismus et al. differ from those obtained by Garibaldi et al. [18], who reported for as-built Fe-Si rings manufactured by L-PBF a maximum total loss of ~ 0.09 J/kg ($J_p = 1.0$ T and $f = 50$ Hz), where the dynamic loss component was very limited. However, it should be considered that the rings investigated by Garibaldi et al. had a higher silicon content (6.9 wt%), which certainly resulted in a higher electrical resistivity. Certainly, dynamic losses in bulk rings represent a very complex and controversial issue. Traditionally, experimental and theoretical studies of eddy currents in soft magnetic materials have mainly concerned laminated samples, and the passage to bulk three-dimensional structures produced by additive manufacturing may not be straightforward. In this respect, additive manufacturing techniques may allow a geometrical manipulation of the internal structure of the printed components, for instance the insertion of air gaps, which appears as a promising method to reduce eddy current losses [26, 62]. However, introducing air gaps in the component also lowers its filling factor, reducing the total flux conducted per unit volume. Pure iron, by virtue of its high J_s and L-PBF feasibility, can be usefully employed as a model material to carry out concept studies in this emerging research field [26].

4 Conclusions

In this paper, the microstructure, mechanical and magnetic behaviour of commercially pure iron manufactured by L-PBF were characterized, both in the as-built (AB) and heat treated (HT) conditions. Preliminarily, the commercially available feedstock powder for L-PBF was characterized in terms of morphology, size distribution and chemical composition. Subsequently, the L-PBF process was optimized to achieve near-full density components (relative density higher than 99%). Samples for microstructural, mechanical and magnetic characterizations were then manufactured and tested in both AB and HT conditions (stress relief annealing at 850 °C for 1 h). The following conclusions can be drawn:

- The present work confirmed the high feasibility of pure iron by L-PBF, as crack-free, high-density samples were manufactured as a result of the performed process optimization.
- The AB microstructure resulted composed of fine (average size of ≈ 5 μm), non-oriented grains of α-Fe with no evidence of melt pools or scan track borders, nor large columnar grains or solidification substructure. No significant difference was observed between vertical and horizontal sections. A dense distribution of sub-micron, spherical particles was observed at high magnification. No appreciable differences in terms of microstructural features were noted after the annealing.
- High hardness and tensile strength were observed in the AB condition, superior to those of conventionally produced pure iron, probably due to the very fine microstructure and the high density of dislocations resulting from the L-PBF solidification conditions. A mild tensile anisotropy was observed, with lower strength and ductility for vertical (90°) specimens, possibly resulting from the presence of defects and residual stresses

due to the L-PBF process. Specimens subjected to the stress relief annealing exhibited lower hardness and tensile strength (still higher than conventionally produced pure iron) and larger ductility, as well as a reduction in the tensile anisotropy, with respect to the AB condition. Since no appreciable microstructural modifications were detected between the AB and HT conditions, these variations were only attributed to the reduction of the dislocation density.

- The magnetic study indicated a magnetic polarization value in line with the nominal one for conventionally produced pure iron, confirming the high purity and density of the L-PBF samples. The magnetic softness, as tested under DC measurement conditions, was definitely enhanced by the annealing treatment due to the reduction of residual stress, as proven by the higher relative permeability and lower coercivity of the HT ring compared to the AB one. However, a larger grain size would be required to further improve the DC soft magnetic performance. The total loss measured in the HT ring, in an AC magnetic field of frequency up to 50 Hz, was smaller than that measured in the AB one (for peak polarization J_p up to 1.0 T) or comparable (for $J_p = 1.5$ T), most likely thanks to the fine-grained structure of the samples, which was not affected by the heat treatment.

To summarize, pure iron manufactured by L-PBF exhibited considerably high mechanical properties, but a satisfactory trade-off between mechanical and magnetic properties appeared difficult to achieve. In particular, the stress relief annealing below the phase transition at 911 °C, tailored to preserve the high mechanical strength of as-built specimens, hindered the possibility of obtaining excellent magnetic softness, which would make the pure iron manufactured by L-PBF especially suitable for DC magnetic applications thanks to its simple processability. Future work will be focused on promoting grain growth by increasing the annealing time without raising the annealing temperature, with the aim of improving the magnetic softness without reducing the mechanical strength.

Funding Open access funding provided by Alma Mater Studiorum - Università di Bologna within the CRUI-CARE Agreement. The research leading to the results in the present work received funding from the 2014–2020 European Regional Development Fund Emilia-Romagna Regional Operational Programme (POR-FESR) under Grant Agreement No. J41F18000050009 (project ACMEC-Additive manufacturing e tecnologie Cyber-physical per la MECcatronica del futuro).

Declarations

Conflict of interest The authors have no competing interests to declare.

References

1. Dietrich DW (1990) Magnetically soft materials. In: Properties and selection: nonferrous alloys and special-purpose materials. ASM International, pp 761–781
2. Lupi S, Rudnev V (2014) Electromagnetic and thermal properties of materials. In: Induction heating and heat treatment. ASM International, pp 28–35
3. ASM International (2006) Blanking and piercing of electrical steel sheet. In: Metalworking: sheet forming, pp 171–176
4. AK Steel International ARMCO® pure iron high purity iron product data bulletin
5. Parrella A, Arpaia P, Buzio M et al (2019) Magnetic properties of pure iron for the upgrade of the LHC superconducting dipole and quadrupole magnets. IEEE Trans Magn 55:1–4. https://doi.org/10.1109/TMAG.2018.2872163
6. (2017) BS EN ISO/ASTM 52900:2017 Additive manufacturing—general principles—terminology
7. Herzog D, Seyda V, Wycisk E, Emmelmann C (2016) Additive manufacturing of metals. Acta Mater 117:371–392. https://doi.org/10.1016/j.actamat.2016.07.019
8. Hebert RJ (2016) Viewpoint: metallurgical aspects of powder bed metal additive manufacturing. J Mater Sci 51:1165–1175. https://doi.org/10.1007/s10853-015-9479-x
9. Frazier WE (2014) Metal additive manufacturing: a review. J Mater Eng Perform 23:1917–1928. https://doi.org/10.1007/s11665-014-0958-z
10. DebRoy T, Wei HL, Zuback JS et al (2018) Additive manufacturing of metallic components—process, structure and properties. Prog Mater Sci 92:112–224. https://doi.org/10.1016/j.pmatsci.2017.10.001
11. Sames WJ, List FA, Pannala S et al (2016) The metallurgy and processing science of metal additive manufacturing. Int Mater Rev 61:315–360. https://doi.org/10.1080/09506608.2015.1116649
12. acatech – National Academy of Science and Engineering, German National Academy of Sciences Leopoldina, Union of the German Academies of Sciences and Humanities (eds) (2017): Additive Manufacturing. Munich, p 64
13. du Plessis A, Broeckhoven C, Yadroitsava I et al (2019) Beautiful and functional: a review of biomimetic design in additive manufacturing. Addit Manuf 27:408–427. https://doi.org/10.1016/j.addma.2019.03.033
14. Hague R, Campbell I, Dickens P (2003) Implications on design of rapid manufacturing. Proc Inst Mech Eng Part C J Mech Eng Sci 217:25–30
15. Sigmund O, Maute K (2013) Topology optimization approaches: a comparative review. Struct Multidiscip Optim 48:1031–1055. https://doi.org/10.1007/s00158-013-0978-6
16. Wein F, Dunning PD, Norato JA (2020) A review on feature-mapping methods for structural optimization. Struct

Multidiscip Optim 62:1597–1638. https://doi.org/10.1007/s00158-020-02649-6
17. Garibaldi M, Ashcroft I, Simonelli M, Hague R (2016) Metallurgy of high-silicon steel parts produced using selective laser melting. Acta Mater 110:207–216. https://doi.org/10.1016/j.actamat.2016.03.037
18. Garibaldi M, Ashcroft I, Lemke JN et al (2018) Effect of annealing on the microstructure and magnetic properties of soft magnetic Fe-Si produced via laser additive manufacturing. Scr Mater 142:121–125. https://doi.org/10.1016/j.scriptamat.2017.08.042
19. Mikler CV, Chaudhary V, Borkar T et al (2017) Laser additive manufacturing of magnetic materials. Jom 69:532–543. https://doi.org/10.1007/s11837-017-2257-2
20. Garibaldi M (2018) Laser additive manufacturing of soft magnetic cores for rotating electrical machinery: materials development and part design. PhD thesis, University of Nottingham
21. Garibaldi M, Ashcroft I, Hillier N et al (2018) Relationship between laser energy input, microstructures and magnetic properties of selective laser melted Fe-6.9% wt Si soft magnets. Mater Charact 143:144–151. https://doi.org/10.1016/j.matchar.2018.01.016
22. Périgo EA, Jacimovic J, García Ferré F, Scherf LM (2019) Additive manufacturing of magnetic materials. Addit Manuf 30:100870. https://doi.org/10.1016/j.addma.2019.100870
23. Bernier F, Ibrahim M, Mihai M et al (2020) Additive manufacturing of soft and hard magnetic materials used in electrical machines. Met Powder Rep 75:334–343. https://doi.org/10.1016/j.mprp.2019.12.002
24. Wu F, El-Refaie AM (2020) Toward additively manufactured electrical machines: opportunities and challenges. IEEE Trans Ind Appl 56:1306–1320. https://doi.org/10.1109/TIA.2019.2960250
25. Plotkowski A, Pries J, List F et al (2019) Influence of scan pattern and geometry on the microstructure and soft-magnetic performance of additively manufactured Fe-Si. Addit Manuf. https://doi.org/10.1016/j.addma.2019.100781
26. Goll D, Schuller D, Martinek G et al (2019) Additive manufacturing of soft magnetic materials and components. Addit Manuf 27:428–439. https://doi.org/10.1016/j.addma.2019.02.021
27. Stornelli G, Faba A, Di Schino A et al (2021) Properties of additively manufactured electric steel powder cores with increased si content. Materials (Basel). https://doi.org/10.3390/ma14061489
28. Chaudhary V, Mantri SA, Ramanujan RV, Banerjee R (2020) Additive manufacturing of magnetic materials. Prog Mater Sci 114:100688. https://doi.org/10.1016/j.pmatsci.2020.100688
29. Lejček P, Roudnická M, Čapek J et al (2019) Selective laser melting of pure iron: multiscale characterization of hierarchical microstructure. Mater Charact 154:222–232. https://doi.org/10.1016/j.matchar.2019.05.012
30. Song B, Dong S, Deng S et al (2014) Microstructure and tensile properties of iron parts fabricated by selective laser melting. Opt Laser Technol 56:451–460. https://doi.org/10.1016/j.optlastec.2013.09.017
31. Letenneur M, Brailovski V, Kreitcberg A et al (2017) Laser powder bed fusion of water-atomized iron-based powders: process optimization. J Manuf Mater Process 1:23. https://doi.org/10.3390/jmmp1020023
32. Palousek D, Pantelejev L, Zikmund T, Koutny D (2017) Processing of nearly pure iron using 400W selective laser melting—initial study. MM Sci J 2017:1738–1743. https://doi.org/10.17973/MMSJ.2017_02_2016184
33. Carluccio D, Bermingham M, Kent D et al (2019) Comparative study of pure iron manufactured by selective laser melting, laser metal deposition, and casting processes. Adv Eng Mater 1900049:1–9. https://doi.org/10.1002/adem.201900049
34. Song B, Dong S, Liu Q et al (2014) Vacuum heat treatment of iron parts produced by selective laser melting: Microstructure, residual stress and tensile behavior. Mater Des 54:727–733. https://doi.org/10.1016/j.matdes.2013.08.085
35. Lejček P, Čapek J, Roudnická M et al (2021) Selective laser melting of iron: multiscale characterization of mechanical properties. Mater Sci Eng A 800:140316. https://doi.org/10.1016/j.msea.2020.140316
36. TLS Technik GmbH. https://www.tls-technik.de/en/home.html
37. ASTM International (2013) Standard test methods for density of compacted or sintered powder metallurgy (PM) products using Archimedes' principle. Astm B962-13 i:1–7. https://doi.org/10.1520/B0962-17.2
38. ASM International (1990) Properties of pure metals. In: Properties and selection: nonferrous alloys and special-purpose materials, pp 1099–1201
39. (2019) BS EN ISO 6892-1:2019 Metallic materials—tensile testing
40. (2021) BS ISO 14707:2021-surface chemical analysis—glow discharge optical emission spectrometry (GD-OES)—introduction to use
41. ASTM International (2012) Standard Guide for preparation of metallographic specimens standard guide for preparation of metallographic specimens. ASTM Int 03.01:1–12. https://doi.org/10.1520/E0003-11R17.1
42. (2014) ISO 10275:2007 Metallic materials—sheet and strip—determination of tensile strain hardening exponent
43. BSI EN ISO 6506-1:2014 Metallic materials—Brinell hardness test
44. Tan JH, Wong WLE, Dalgarno KW (2017) An overview of powder granulometry on feedstock and part performance in the selective laser melting process. Addit Manuf 18:228–255. https://doi.org/10.1016/j.addma.2017.10.011
45. ASM International (2004) Solidification Structures of Pure Metals. In: Metallography and Microstructures, pp 93–96
46. ASTM International (2010) Standard test methods for determining average grain size. ASTM Int. https://doi.org/10.1520/E0112-13.1.4
47. ASM International (2004) Fundamentals of solidification. In: Metallography and microstructures, pp 71–92
48. ASM International (1993) Fundamentals of weld solidification. In: Welding, brazing and soldering, pp 45–54
49. Saeidi K, Gao X, Zhong Y, Shen ZJ (2015) Hardened austenite steel with columnar sub-grain structure formed by laser melting. Mater Sci Eng A 625:221–229. https://doi.org/10.1016/j.msea.2014.12.018
50. Liverani E, Toschi S, Ceschini L, Fortunato A (2017) Effect of selective laser melting (SLM) process parameters on microstructure and mechanical properties of 316L austenitic stainless steel. J Mater Process Technol 249:255–263. https://doi.org/10.1016/j.jmatprotec.2017.05.042
51. Zhong Y, Liu L, Wikman S et al (2016) Intragranular cellular segregation network structure strengthening 316L stainless steel prepared by selective laser melting. J Nucl Mater 470:170–178. https://doi.org/10.1016/j.jnucmat.2015.12.034
52. Smallman RE, Ngan AHW (2014) Work hardening and annealing. In: Modern physical metallurgy. Elsevier, pp 443–471
53. Fang Z-C, Wu Z-L, Huang C-G, Wu C-W (2020) Review on residual stress in selective laser melting additive manufacturing of alloy parts. Opt Laser Technol 129:106283. https://doi.org/10.1016/j.optlastec.2020.106283
54. Fiorillo F (2004) Characterization and measurement of magnetic materials. Elsevier, Amsterdam

55. Ferrara E, Olivetti E, Fiorillo F et al (2014) Microstructure and magnetic properties of pure iron for cyclotron electromagnets. J Alloys Compd 615:S291–S295. https://doi.org/10.1016/j.jallcom.2014.01.217
56. Cullity BD, Graham CD (2009) Introduction to magnetic materials. IEEE Press, Wiley, Hoboken
57. Landgraf FJG, Emura M (2002) Losses and permeability improvement by stress relieving fully processed electrical steels with previous small deformations. J Magn Magn Mater 242–245:152–156. https://doi.org/10.1016/S0304-8853(01)01184-2
58. Degauque J, Astie B, Porteseil JL, Vergne R (1982) Influence of the grain size on the magnetic and magnetomechanical properties of high-purity iron. J Magn Magn Mater 26:261–263. https://doi.org/10.1016/0304-8853(82)90166-4
59. Chin GY, Wernick JH (1980) Chapter 2 Soft magnetic metallic materials, pp 55–188
60. de Campos MF, Teixeira JC, Landgraf FJG (2006) The optimum grain size for minimizing energy losses in iron. J Magn Magn Mater 301:94–99. https://doi.org/10.1016/j.jmmm.2005.06.014
61. Tiismus H, Kallaste A, Belahcen A et al (2020) Hysteresis measurements and numerical losses segregation of additively manufactured silicon steel for 3D printing electrical machines. Appl Sci 10:6515. https://doi.org/10.3390/app10186515
62. Tiismus H, Kallaste A, Belahcen A et al (2021) AC magnetic loss reduction of SLM processed Fe-Si for additive manufacturing of electrical machines. Energies 14:1241. https://doi.org/10.3390/en14051241